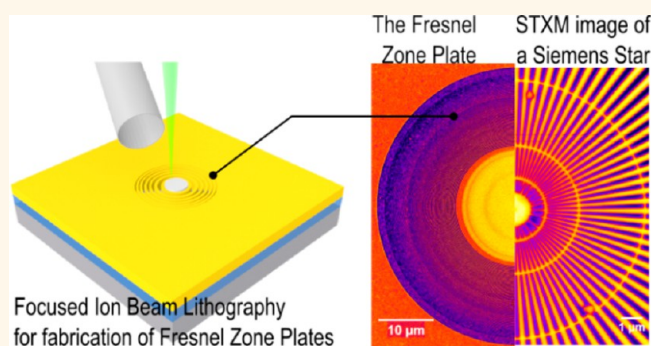# Rapid Prototyping of Fresnel Zone Plates *via* Direct Ga⁺ Ion Beam Lithography for High-Resolution X-ray Imaging

Kahraman Keskinbora, Corinne Grévent,* Ulrike Eigenthaler, Markus Weigand, and Gisela Schütz

Max Planck Institute for Intelligent Systems, Heisenbergstrasse 3, D-70569 Stuttgart, Germany

ABSTRACT A significant challenge to the wide utilization of X-ray microscopy lies in the difficulty in fabricating adequate high-resolution optics. To date, electron beam lithography has been the dominant technique for the fabrication of diffractive focusing optics called Fresnel zone plates (FZP), even though this preparation method is usually very complicated and is composed of many fabrication steps. In this work, we demonstrate an alternative method that allows the direct, simple, and fast fabrication of FZPs using focused Ga⁺ beam lithography practically, in a single step. This method enabled us to prepare a high-resolution FZP in less than 13 min. The performance of the FZP was evaluated in a scanning transmission soft X-ray microscope where nanostructures as small as sub-29 nm in width were clearly resolved, with an ultimate cutoff resolution of 24.25 nm, demonstrating the highest first-order resolution for any FZP fabricated by the ion beam lithography technique. This rapid and simple fabrication scheme illustrates the capabilities and the potential of direct ion beam lithography (IBL) and is expected to increase the accessibility of high-resolution optics to a wider community of researchers working on soft X-ray and extreme ultraviolet microscopy using synchrotron radiation and advanced laboratory sources.

The Fresnel Zone Plate | STXM image of a Siemens Star | Focused Ion Beam Lithography for fabrication of Fresnel Zone Plates

X-ray microscopy is a nanoimaging technique with unique abilities to work under a variety of ambient conditions, imaging in real space with high temporal[1–5] and spatial resolutions[6–8] combined with chemical analysis capabilities[9] and unique contrast mechanisms[10,11] even magnetic contrast.[12] While the technique has long been considered to be confined to synchrotron radiation sources, recent developments have led to the introduction of new laboratory X-ray sources and microscopes,[13–18] improving its accessibility and rendering its technical components highly desirable to a broader community.[14,19,20] Basically, the Fresnel zone plate (FZP) is inevitably the core element behind high-resolution X-ray and extreme ultraviolet imaging. A FZP is a diffractive optic capable of focusing high energy electromagnetic radiation. In its simplest form, it is a concentric set of alternating transparent and absorbing rings (*i.e.*, zones), with radial positions following the zone plate law,[21] $r_n = (n\lambda f + n^2\lambda^2/4)^{1/2}$, where r_n is the zone radius, n is the zone index, λ is the wavelength, and f is the focal length. A FZP with a large number of zones behaves like a simple lens[22] and focuses X-rays alleviating the problems regarding high absorption of extreme ultraviolet (XUV) and soft X-rays (SXR) within matter. The diffraction limited resolution of a FZP in the focus of first diffraction order, considering the Rayleigh criterion, is given by $\delta_{Rayleigh} = 1.22\Delta r$, where Δr is the outermost zone width.[23] Accordingly, in order to increase the resolution of the first order focus, FZPs with smaller Δr have to be fabricated which is a very demanding nanotechnology challenge.

The fabrication process for FZPs with high resolution became accessible after 1971, as

TABLE 1. Overview of the IBL–FZP Attributes from the Prior Literature Compared to the Present Work (Column F)[a]

		A	B	C$_1$	C$_2^+$	D	E$_1$	E$_2$	F
	Year	2001	2007	2011		2012	2012		2013
FZP Parameters	FZP Material	TaSiN	Ni	Cr		Au	Au$_{0.8}$Pd$_{0.2}$		Au
	D [μm]	60	15	50	70	100	96	92.3	50
	h [nm]	1000	300	50		500	113	260	110
	Δr [nm]	170	100	129	90	100	120		50
	S [μm^2]	2375	177	1964	3848	7854	6577	6510	1583
Experimental FZP Performance	Imaging Performed	No (wire scan)	No	No		Yes	Yes		Yes
	$\delta_{measurement}$ [nm]	540	-	-	-	120	172	189	57
	DE [%] at 900 eV	n/a	n/a	n/a	n/a	~7*	n/a	n/a	2.75
Ion Beam Parameters	FIB V [kV]	50	30	30		40	30		30
	FIB I [nA]	1.2	0.08	0.01		0.05	0.074	0.053	0.03
Fabrication Time	t [min]	**107**	**60**	**540**	**840**	**900**	**210**	**510**	**13**
	Relative Fab. Time	0.6	15.1	73.7	58.5	3.1	3.8	4	1

[a] A: Ilinski et al.[47] B: Surpi et al.[48] C: Lenz et al.[50] D: Nadzeyka et al.[39] E: Overbuschman et al.,[49] F: present work. $^+$In the case of C$_2$ only a few outer zones are milled; time and area given are for a full FZP. *From Keskinbora et al.[40] Key: D, diameter of the FZP; h, FZP structure height; Δr, outermost zone width; S, approximate active FZP area (evaluated inactive central portion determined from published images subtracted if relevant); $\delta_{measurement}$, measured full-period resolution (not cutoff); DE, measured diffraction efficiency; V, acceleration voltage; I, ion beam current; t, fabrication time (FIB milling) in minutes; rel fab time, fabrication time relative to the present work taking thickness and active areas into account (active FZP surface area × FZP height/milling time, normalized to present study).

Sayre suggested[24] the use of their then-recently developed e-beam lithography (EBL) system to prepare FZPs. Over the last four decades, the fabrication of FZPs via EBL improved remarkably. Today, using fabrication schemes of increasing complexity, it is even possible to resolve structures smaller than 10 nm with SXR using FZPs,[6−8] but such a high resolution requires highly specialized and sophisticated equipment as well as advanced technical knowledge that are not readily available. On the practical side, common EBL–FZPs can resolve features of 20 down to 15 nm. An important drawback when using EBL to prepare FZPs is that it relies on at least four[21] or more[25−28] fabrication steps depending on the properties of the FZP. These complicated procedures require effort and time; thus, costs can quickly escalate,[29] not to mention the accumulation of errors through each step, again impacting on its final quality. Finally, as EBL process time is considered, various figures are reported in the literature such as up to 30 min for a single baking step[7] and etch times anywhere from 5 min[6] up to 14 h[30] depending on the desired depth.

Here, we show a new process based on ion beam lithography (IBL) that allows the rapid fabrication of FZPs, in 13 min, in a single patterning step. As IBL implies the direct writing of patterns, it advantageously enables the prototyping of micro- and nanosystems[31] in a single step. It potentially circumvents the inherent drawbacks of other nanolithography approaches such as the proximity effect in EBL.[32−37] While it was considered to be slow,[34,38] exotic,[33] and underdeveloped,[34−36] the recent progress in advanced focused ion beam (FIB) tools and processes are extremely promising. Incomparable capabilities were developed and are ranging from higher acceleration voltages and optimized beam correction systems with precise interferometrically controlled sample stages[39,40] to other systems capable of writing features as small as 10 nm with 30 nm periodicity[41] and processing of large write fields[42] as well as development of He$^+$ ion microscopes[43] toward sub-10 nm[44,45] down to 4 nm[45,46] patterning. In the case of direct milling IBL, the overall smaller number of process steps means that the required expertise field is narrower which makes the process optimization easier and lowers the potential number of fabrication errors. After the very first studies on fabrication of FZP with IBL,[47,48] the first imaging trials of real objects were reported as recently as 2012 with IBL–FZPs possessing 120 nm[49] and 100 nm[39] Δr. Thus far, required structuring times of 1 h,[48] 1.8 h,[47] 3.5−8.5 h,[49] 9−14 h,[50] and 15 h[39] for the IBL–FZPs were reported. The reported fabrication time varies significantly from one study to another

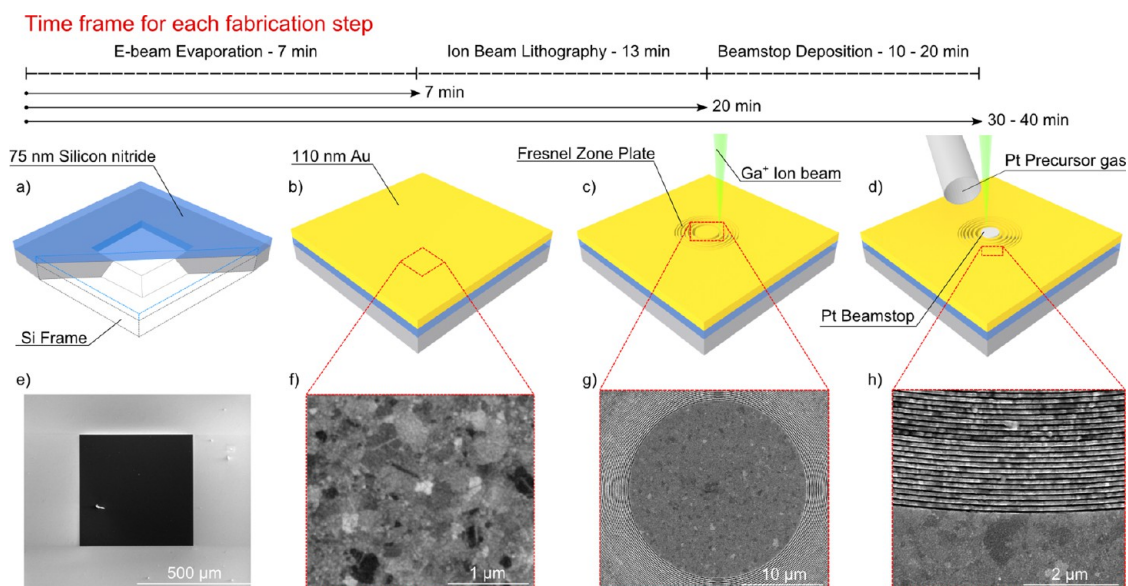Time frame for each fabrication step

Figure 1. Overview of the fabrication process (not to scale). Top row: time required for each fabrication step and overall process time. Middle row: schematic representation at each fabrication step: (a) Cut-away view of the substrate, (b) Au film on the membrane, (c) a FZP is being machined in the Au layer, and (d) *in situ* deposition of the Pt beamstop. Bottom row: SEM images at each step: (e) window area, (f) microstructure of the Au film, (g) central portion of the FZP after IBL processing, and (h) outermost part of the IBL−FZP. All SEM images are taken under normal incidence.

depending on the patterning parameters, the choice of materials, and the FIB and FZP parameters. In our approach, the total fabrication time has been reduced to 13 min (see Table 1), compromising neither the light collection capability of the FZP (*i.e.*, the diameter and the active area of the FZP) nor substantially reducing its diffraction efficiency in the extreme UV and soft X-ray range (theoretically 7.8% at 1200 eV for the present 110 nm thick FZP versus 10.4% for a 500 nm thick Au IBL−FZP, reported previously[39]). Interestingly, the results were obtained on a standard multipurpose Dual-Beam FIB device and rely essentially on the development and optimization of an advanced milling strategy which is observed as a critical component for a successful fabrication scheme. This and the emergence of high-performance IBL systems as mentioned above, therefore, suggest very positive developments for the future. The proper function of the IBL−FZP was tested with a state of the art soft X-ray scanning transmission microscope (STXM) demonstrating a high performance by resolving structures down to 28.5 nm, with an ultimate cutoff resolution of 24.25 nm. This result effectively doubles the resolution achieved for any IBL−FZP reported up to now; it brings IBL−FZP to resolution ranges that are comparable to those of commercial EBL−FZPs while offering a competitive processing time, a simplified process, a significant reduction of required skills, and optimization efforts and corresponding reduced costs.

RESULTS AND DISCUSSION

Fabrication of the FZP and the Resulting Structure. A FZP of 50 μm diameter, 50 nm outermost zone width, and ∼110 nm thickness was prepared using a focused

Ga$^+$ ion beam generated by a general purpose dual beam FIB system, as per the following procedure. A 75 nm thick, X-ray transparent, amorphous silicon nitride membrane on silicon was selected as a substrate (Figure 1a,e) which was coated with a 110 nm thick gold layer (Figure 1b) *via* electron beam evaporation. The evaporation process took approximately 7 min and resulted in a fine-grained Au thin film without introducing any strain in the window area (Figure 1f). Gold was chosen as the absorbing material as it exhibits favorable properties both for X-ray microscopy and FIB micromachining. Being a highly absorbing material, Au gives reasonable diffraction efficiencies over a wide range of photon energies. In addition, when irradiated with 30 keV Ga$^+$ ions under normal incidence, Au has a sputtering yield, Y, of 17.35 atoms/ion, according to SRIM[51,52] simulations (see the Supporting Information, Figure S1) or 15.75 to 14.7 atoms/ion according to the literature.[53,54] These values correspond to volume sputtering rates per dose, B, of 1.84, 1.67, and 1.56 in μm^3/nC, respectively. This high sputtering rate makes it easier to quickly remove large areas of the material *via* IBL, a very important attribute as it is one of the crucial parameters which defines the overall process time, t, in accordance with the following relationship

$$t \text{ (s)} = \frac{V(\mu\text{m}^3)}{I(nC/s) \cdot B(\mu\text{m}^3/nC)} + t_{DC} \text{ (s)} \qquad (1)$$

where the first term of the right-hand side of eq 1 is taken from the work of Hopman *et al.*,[55] V is the volume to be sputtered, I is the ion beam current, and t_{DC} is the time spent for drift correction.

For patterning, a Ga$^+$ ion beam with 30 keV energy and 30 pA current was employed that resulted in a nominal beam size of 16 nm which was aligned for astigmation prior to the patterning in an area just outside of the membrane window. The FZP pattern was written with 10 nm steps, resulting in an overall dosage of 0.03 nC/μm^2 starting from the outermost zone and moving the beam toward the center (Figure 1c) in a circular trajectory until a predetermined radius ($\sim$11 μm) was reached. It resulted in 102 open zones, and all the inner zones from that point on were left nonmachined. This corresponds to $\sim$88 μm^3 of material that was milled away. No drift correction scheme was employed in the process; hence, t_{DC} was 0. According to eq 1, the overall process time can be estimated to range between approximately 26.6 and 31.5 min. Nevertheless, when utilizing the above given experimental parameters, the IBL−FZP was milled in only 13 min (Figure 1g). The difference between the actual process and the calculation is attributed to uncertainties in the real sputter rate, the Au thin films density and thickness, as well as redeposition and channeling effects.[53] During the milling, the beam direction was changed from clockwise (cw) to counter clockwise (ccw) and *vice versa* for each successive open zone. These precautions were taken to avoid any dynamical beam movement effects, and to minimize the impact of the redeposition process, *e.g.*, to avoid any unidirectional redeposition, which degrades the quality of the structure.

Since the zone placement accuracy is a local requirement for each zone (for instance 0.7Δr_n tolerance in radius for avoiding astigmatism),[56,57] it is less stringent for the inner and wider zones. Hence by starting the process from the outermost zones, which are the most important for the resolution and also most vulnerable to the misplacement, the impact of the drift on the zones was reduced to a minimum; it even avoided the drift correction process which was necessary in some other studies;[26,29] more so, it improved the overall process time. Experimentally, the total average drifts of 76.6 and 83.3 nm during the whole fabrication process were measured for the vertical and the horizontal directions, respectively corresponding to the misplacement of the innermost zone. Moreover, an uncertainty in the beam placement after each drift correction step is reported in the past, which varies between about 20[39,50] up to 60[45] nm. Therefore, avoiding a drift correction step might actually improve the zone placement accuracy given that the process is completed in a timely manner. Overall, the following parameters were found to be crucial for the successful preparation of the IBL−FZP: first, the dosage needed to be high enough to remove material from zones in one pass without damaging the underlying membrane; second, the beam current was optimized
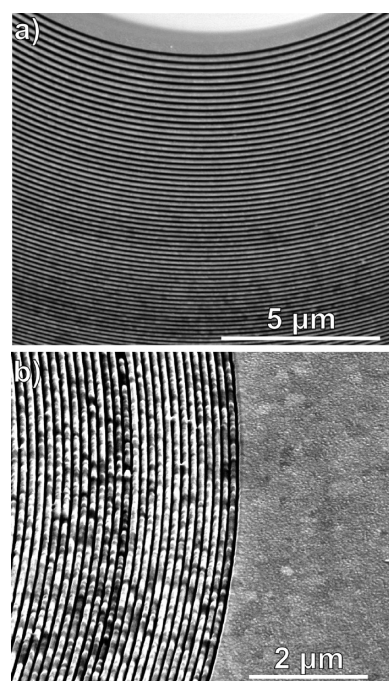

Figure 2. SEM images of the fabricated FZP: (a) innermost zones under normal view, (b) outermost zones viewed under 52° tilt.

to ensure both a reasonable process time and a high accuracy; and third, the material was chosen providing both a high sputter yield and a proper microstructure.

The nonmilled part in the center of the IBL−FZP provided a platform for the beamstop deposition. This initial platform blocks about 74% of 900 eV photons (see Figure S2, Supporting Information) or lower, as thin films usually have a lower density than their bulk counterparts. Without a proper beamstop, the remaining light would create a significant background in the detector signal reducing the maximum achievable contrast. Therefore, an additional layer of Pt was deposited on this platform *in situ* by successive electron and focused ion beam induced depositions (EBID and FIBID), respectively, (Figure 1d) which took 10−20 min depending on the selected parameters.

The resulting FZP exhibited a high overall quality (Figure 2a,b), which is remarkable considering the short milling time of only 13 min. The relatively rough surface of the outermost zones as observed by SEM imaging (Figure 2b), is attributed to the grain structure of the polycrystalline Au thin film which could be improved by employing a single crystalline or amorphous thin film material. Since the amorphous nature of the underlying membrane would make the former option practically unfeasible, the latter would be a better choice. This can be achieved by cosputtering an alloy instead of a pure metal and it is under consideration in future studies. Nevertheless, the zones have a clearly defined structure. The intended
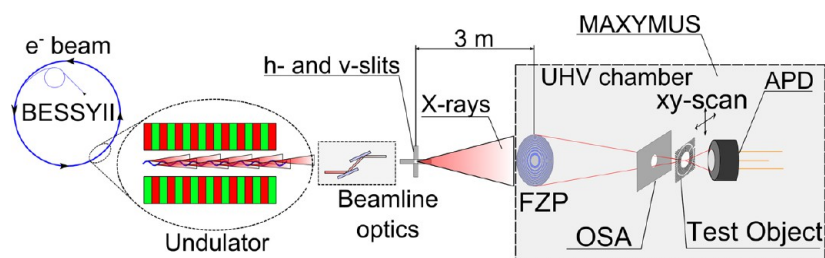
Figure 3. Schematic representation of the scanning transmission X-ray microscope MAXYMUS. Undulating relativistic e^- emit highly coherent X-rays which are monochromatized *via* a plane grating monochromator (PGM) and in combination with a set of slits, defines the spatially coherent, monochromatic, plane wave illumination of the FZP. The desired diffraction order of the FZP is selected by a circular order-selecting aperture (OSA). The sample, located at the focal plane, is scanned through the focus, and the transmitted X-rays are collected *via* an avalanche photodiode (APD) point detector. The laser interferometry controlled sample stage in combination with a very effective dampening system of the microscope allows for a very high-resolution imaging.
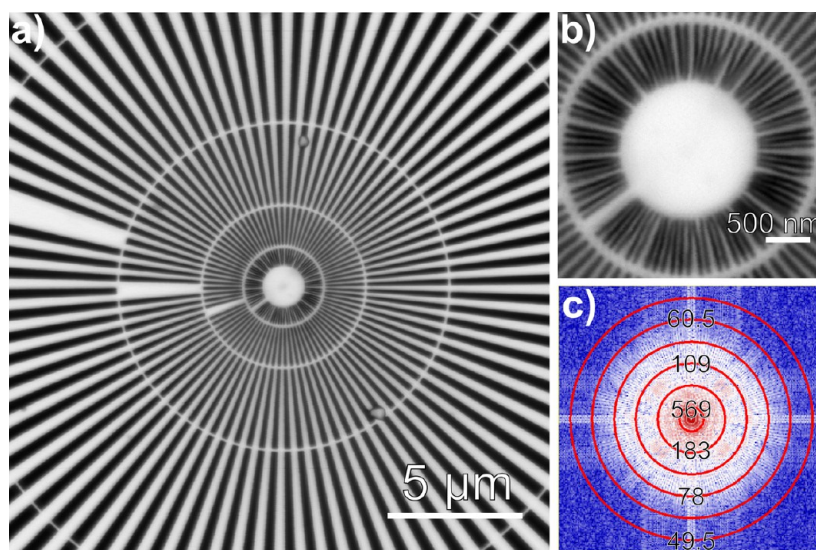

Figure 4. (a) Line-by-line STXM image of the Siemens star taken at 701 eV, 10 nm step, 0.34 ms dwell time. (b) Point-by-point scan under fully coherent illumination at 901 eV, 10 nm step size, and 5 ms dwell time. (c) FFT of image shown in (b); concentric circles and corresponding spatial frequency in nm are overlaid on to the FFT.

line-to-space ratio (L:S) of the design was 1:1. However, due to the redeposition processes that occurs in the wake of the ion beam, the resultant outermost L:S was measured to be approximately 3:2. Another deviation from the ideal FZP structure is the decreasing height of the zones from 110 nm for the inner zones to about 50 nm toward the outermost zones. In addition, the zone walls present an inclined wall structure, characteristic of narrow structures fabricated by FIB (Figure S3, Supporting Information).[39,47] This particularity of the IBL–FZP was already shown to allow for second order imaging at high resolution.[40]

Table 1 shows the fabrication and design parameters for the IBL–FZPs reported so far in the literature compared to the IBL–FZP reported here. The relative fabrication time (row 14 of Table 1) allows a comparison between the various methods. It takes the FZP thickness and active area into account normalized to the present study. Ilinski *et al.*'s work was the fastest according to this analysis, which is understandable considering the high acceleration

voltage and current that was used in the study. However, the experimental resolution was more than 9 times lower than in the present study. In our approach the relative fabrication time was more than 3 times shorter than for the FZP with the closest reported first order resolution (column D), which has a factor of 2 lower resolution. Moreover, the results of column D in Table 1 were realized with a state of the art IBL system working at an acceleration voltage of 40 keV whereas in the present study, a standard multipurpose FIB workstation DualBeam (FEI) was employed at 30 keV without interferometric stage control. These results underline the future potential wide applicability of the IBL technique to the X-ray optics fabrication.

Resolution of the IBL–FZP. The resolution of the IBL–FZP was tested in the SXR range. For this purpose, it was mounted as focusing optic in the scanning transmission X-ray microscope (STXM) MAXYMUS,[58] located at the BESSY II synchrotron radiation facility, which is schematically described in Figure 3. Two different, standardized

Figure 6. Diffraction efficiency map of a gold FZP with rectangular profile calculated according to the thin grating approximation for various thicknesses and photon energies. A high efficiency region is positioned just below 200 eV and is important for XUV imaging.
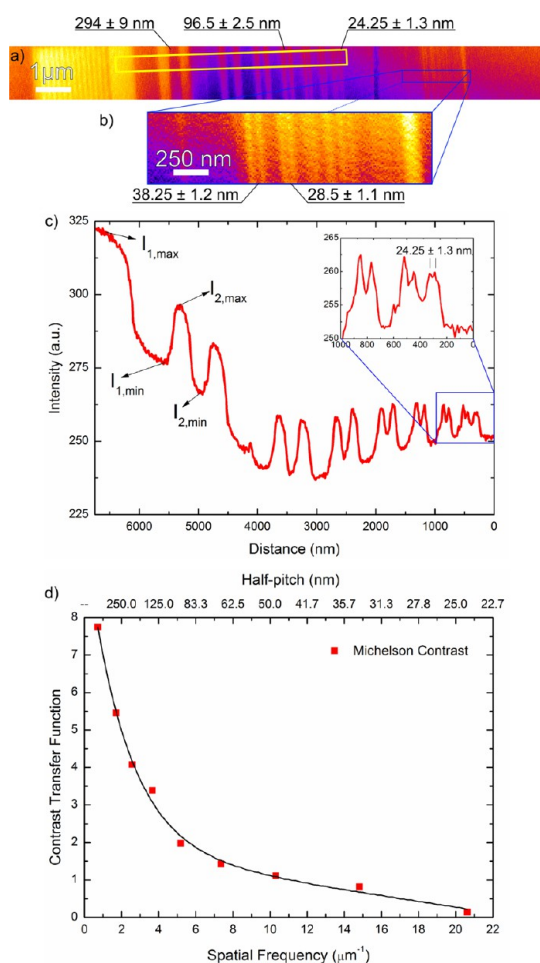
Figure 5. (a) Line-by-line STXM image of the multilayer test object at 1120.6 eV, 10 nm step size, 0.42 ms dwell time. Certified half-pitch structure sizes along with uncertainties are given above the image. (b) Point-by-point STXM image of the portion of the test structure showing smallest structures acquired at approximately 1120 eV, 10 nm step size 10 ms dwell time. Certified half-pitch structures sizes with uncertainties are given below the image. (c) Integrated intensity across the short axis of the marked rectangle in (a) as a function of distance normal to the layer interfaces. The inset is a zoom in to the rightmost three periods (d) CTF of the IBL−FZP as determined from (c) shown as a function of spatial frequency and structure size. The solid line is a least-squares fit of the data points and is given as an eye guide.

test objects, a Siemens star and a GaAs/Al$_{0.7}$Ga$_{0.3}$As multilayer, were utilized as samples to assess the resolution of the IBL−FZP.

The absorption contrast image of the Siemens star test pattern was obtained by utilizing the present IBL−FZP as the focusing optic in MAXYMUS and is shown in Figure 4a. For the acquisition, the h- and v-slits were opened to 50 × 50 μm enabling enough light for the line-by-line scanning of the 2000 × 2000 pixels image in about 23 min. In Figure 4a, it can be seen that even the smallest, 30 nm structures of the innermost ring in the test pattern can be resolved with a high contrast in every direction without any distortion. This demonstrates the absence of a significant degree of optical aberration, as, for instance,
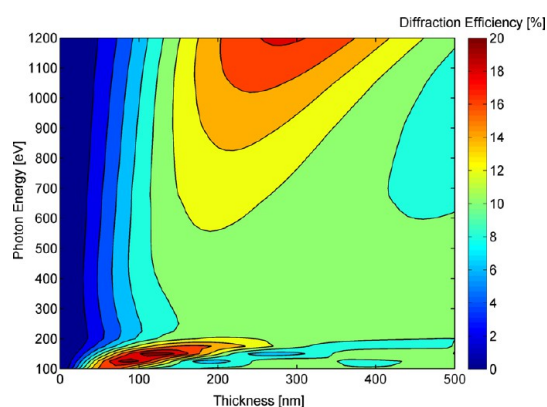
astigmatism of the FZP that might have resulted from the fabrication scheme avoiding a drift correction. The slits were then closed to 15 × 15 μm ensuring the fully coherent illumination of the IBL−FZP and a diffraction limited focal spot size. A point-by-point scan of the innermost ring of the Siemens star test pattern was performed (see Figure 4b.) The innermost ring of the Siemens star with the smallest local feature size of 30 nm (60 nm period) is clearly resolved. Figure 4c shows the power spectrum of the fast Fourier transform (FFT) of the image shown in Figure 4b. In Figure 4c, the spatial frequency increases radially outward, i.e., the structure size, indicated by the overlaid circles in Figure 4c, decreases, while the intensity also decreases until it disappears into the background when the frequency corresponding to the smallest resolvable structure size is achieved.[59,60] Here, the signal disappears at about 60.5 nm per period; i.e., features of 30.25 nm width are resolvable. This value is comparable to the smallest features of the test pattern (30 nm) and is attributed to the size limit of the test pattern and not to the ultimate resolution of the FZP.[59]

For further determination of the resolution, a second test object, a 500 nm thick lamellae from a GaAs/Al$_{0.7}$Ga$_{0.3}$As multilayer with certified (by BAM, see the Materials and Methods) layer thicknesses,[6] was imaged. As the thinnest features in the multilayer structure are far smaller than the resolution of the IBL−FZP, it is well suited for the determination of the ultimate resolution. Imaging was carried out at 1120.6 eV, in the vicinity of gallium absorption edge to maximize the contrast. A line-by-line image of the complete structure with 10 nm pixel size (Figure 5a) was recorded, as well as a point-by-point image of the thinnest layers (Figure 5b). The image shown in Figure 5b demonstrates that the 28.5 ± 1.1 nm lines and spaces are just resolvable. Note that the decreasing efficiency of the FZP at 1200 eV (7.8% theoretically) causes the high noise in Figure 5b. From the image in Figure 5a,
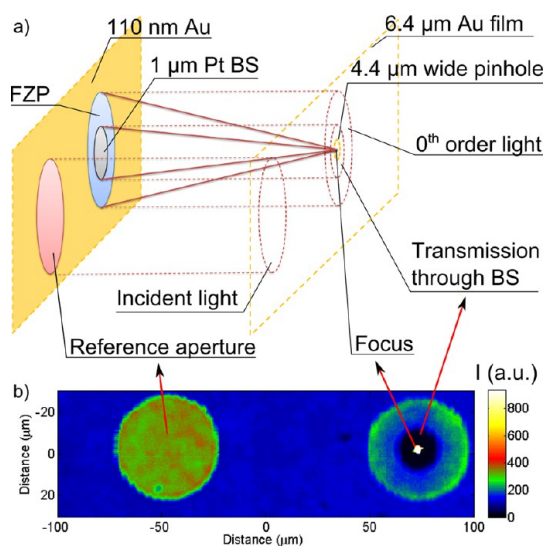
Figure 7. (a) Experimental setup that was used for the determination of the diffraction efficiency is shown schematically (BS: beamstop). (b) Line-by-line scan of the pinhole spanning over a 60 by 200 μm wide area showing the reference aperture (left) as well as the IBL−FZP (right). High intensity of the focus can be seen clearly.

the contrast transfer function (CTF) of the lens was determined by first integrating the image intensity (Figure 5c) across the short axis of the marked rectangle (Figure 5a) and calculating the CTF following the definition of Michelson contrast,[61] CTF = $(I_{max} - I_{min})/(I_{max} + I_{min})$. The CTF shown in Figure 5d (see also the Materials and Methods) demonstrates the capability of the IBL−FZP to transfer a nonzero contrast for structures as small as 24.25 ± 1.3 nm. This measured cutoff resolution is very close to the theoretical cutoff half-pitch resolution given by the Sparrow resolution limit[62] ($0.95\Delta r_n/2 = 23.75$ nm). This demonstrates the high performance of the IBL−FZP which is due to the high precision of the fabrication process.

Diffraction Efficiency of the IBL−FZP. Fresnel zone plates direct light into several diffraction orders creating a series of foci along optical axis at distances $f_m \approx D\Delta r/\lambda m$, where D is the diameter of the FZP and m the diffraction order. Each of these foci contains some part of the incoming power, the ratio of which to the light incident on the FZP defines the diffraction efficiency (DE) of that particular order. The DE depends on many parameters such as the energy-dependent complex refractive index and the geometry of the FZP. In this work, the geometry of the design FZP was a rectangular zone profile with 1:1 line-to-space ratio. The DE of such a FZP can be analytically calculated via either the thin grating approximation which is valid for a FZP with a low aspect ratio[63] or for instance the coupled wave theory for thicker FZPs.[64−66] Here, the thin grating approach is valid and was utilized. The DE map as a function of the structure thickness and the photon energy of the IBL−FZP is shown in Figure 6. In the energy range between 200 and 1200 eV, the

theoretical DE varies from a minimum of 7.8% at 1200 eV to a maximum of 9.7% at 675 eV for the 110 nm thickness chosen for the design which is suitable for efficient imaging. Moreover, there is a very efficient region in the DE map, just below the 200 eV in the vicinity of 110 nm thickness (DE up to more than 20%) and makes the present FZP markedly relevant and important for the laboratory based sources that exist and currently being developed for this particular energy range.[17,67,68]

To determine the DE of the actual IBL−FZP device experimentally, a separate setup was devised and is shown in Figure 7a. An aperture of approximately the same diameter as the IBL−FZP, serving as a reference for the incoming intensity, was milled in the substrate approximately 125 μm away from the IBL−FZP (center-to-center distance) using FIB. A 4.4 μm wide pinhole was milled on a separate 6.4 μm thick gold film on a silicon nitride membrane. The latter was positioned in the first-order focal plane of the IBL−FZP (Figure 7a) blocking any incoming X-ray except through the pinhole. The pinhole was then raster scanned in the focal plane, spanning the reference aperture and the IBL−FZP to deliver an image where each point corresponds to the light passing through the pinhole at that given position (Figure 7b). For the estimation of the DE, the measured transmission through the beamstop was subtracted from the intensity at the focus (focal intensity). The ratio of this focal intensity to the amount of X-ray light incident on the active area of the FZP gives the value of DE. At 900 eV, the DE was found to be 2.6% for the whole device (including the membrane) and 2.75% for the IBL−FZP itself (corrected for the membrane absorption). The difference in the theoretical and experimentally determined values of the DE is attributed to the deviations of the FZP structure from the ideal, that is, slanted wall profile which decreases the theoretical DE to 8.7% from 9.3% (about 5% decrease compared to the rectangular),[63] the lower thickness and the rough surface of the outermost zones of the IBL−FZP, nonideal line-to-space ratio (Figure S3, Supporting Information), the uncertainties in the density of the evaporated gold as well as the 5−10% spatial variation in the detection efficiency over the APD surface.

CONCLUSIONS

A FZP for high-resolution X-ray microscopy was fabricated in 13 min with ion beam lithography. It was successfully employed as a focusing optic in a scanning X-ray microscope where it resolved nanostructures as small as sub-29 nm in width, with good contrast. The ultimate cutoff resolution was determined to be of approximately 24.25 ± 1.3 nm. The diffraction efficiency of the IBL−FZP was determined to be 2.75% at 900 eV.

With this new and improved fabrication scheme the preparation time of IBL−FZPs in relation to the surface

area, height, and comparable IBL parameters was reduced by a factor of 3.1 to 73.7, implying a significant reduction of costs while at the same time the first-order resolution was improved by a factor of 2.[39,48−50]

Exciting enough, the results were obtained not with state of the art IBL/FIB devices such as the helium ion microscope[69] or a dedicated IBL system[39,40,42] but rather with a general purpose focused ion beam device operated at a moderate acceleration voltage of 30 kV and, hence, a machine that is relatively easily accessible. The results point out to the vast potential of the IBL. The resolution of the ion beam lithographic FZP is only a factor of approximately 2 lower than those obtained with up to date electron beam lithography systems operated at high voltage.[7,8] Recent progresses and successful development of X-ray laboratory microscopes[14,70] and sources[15,16] pave the way to a foreseeable spread of X-ray microscopy to a wider community. It is worth noting that the method described here is fast and flexible implicating a low number of fabrication steps and required skills.

Interesting developments in new ion sources[43,71,72] and high precision IBL systems working at higher acceleration voltages[39,40] are being made each day. It has been already demonstrated that these FIB systems can achieve dense pattern resolution as low as 4 nm[46] which is better than the best achieved by EBL.[73] Further positive impacts on the fabrication of high resolution diffractive optics for SXR and XUV and on other fields such as materials science and engineering,[74] nano/micro electro mechanical systems,[75] plasmonics,[76−78] micro-optics,[79,80] etc. are to be expected.

MATERIALS AND METHODS

Deposition of the Au Layer. A bare, amorphous silicon nitride membrane with a thickness of 75 nm and a window area of 500×500 μm was used as a substrate (Silson Ltd., UK). 110 nm of Au was deposited on the substrate directly *via* e-beam evaporation. The base pressure was 6.3×10^{-7} mbar, and the deposition rate was approximately 2.6 Å/s. The actual deposition took approximately 7 min with a pump down time of ∼3 h. Electron beam evaporated gold layers were free of residual stress and distortion in the window area.

Focused Ion Beam Lithography. The resulting bilayer structure was surface micromachined using a focused Ga^+ ion beam in a dual-beam microscope (Nova 600 NanoLab DualBeam, FEI, The Netherlands), precisely removing the gold from desired positions and leaving the underlying membrane intact. This was achieved by carefully optimizing the patterning parameters. Widths and radial positions of the zones were calculated following the zone plate formula, that is, $r_n = (n\lambda f + n^2\lambda^2/4)^{1/2}$ and used to generate the design pattern, a computer-generated GDSII file, which consists of only ring shaped curved elements that make up the zones of the FZP. This design pattern was fed to the dual-beam FIB using a dedicated pattern generator (ELPHY Multibeam, Raith GmbH, Germany) with a 16 bit patterning capability. An ion beam of 16 nm nominal spot size at 30 kV and 30 pA was used to write the pattern using 10 nm isometric steps, which gives a 37.5% beam overlap. A dwell time of 0.1 ms was utilized which in combination with other parameters resulted in a dosage of 0.03 nC/μm^2 and a beam speed of 0.1 mm/s. Rings of the pattern were written in a circular fashion starting from the outermost zone moving toward the center while stepping in radial direction within each zone also toward the center. In addition, each open zone was written in an antiparallel direction to its neighbors, *i.e.*, ...clockwise/counter cw/clockwise... and starting points 180° apart from each other. These precautions ensured avoiding any dynamical effects which may result from concentric beam movement. The first 23 even zones in the center were left unmilled so that there is a platform of 110 nm thick Au and 75 nm thick silicon nitride membrane. This ∼22 μm diameter platform in the center of FZP which was covered *in situ* by 1 μm thick Pt layer forming a beamstop to block zeroth order transmission. Trimethyl-(cyclopentadienyl)platinum(IV), $(CH_3)_3CH_3C_5H_4Pt$, was utilized as the metal−organic precursor gas. First, a thin seed layer of Pt was deposited *via* EBID to avoid any damage to the FZP. Then, a second and thicker layer of Pt was deposited *via* FIBID. The thickness of the resulting Pt beamstop was approximately 1 μm on its thickest point.

Efficiency Calculations. Theoretical diffraction efficiencies of the fabricated devices were calculated using the geometrical approach developed by Kirz[63] for a rectangular FZP profile having 1:1 L:S ratio. These calculations are based on a thin grating approximation which is valid for low aspect ratio FZPs, e.g., the present IBL−FZP.

Soft X-Ray Microscopy. The fabricated Fresnel zone plate was tested in the soft X-ray range using the scanning transmission X-ray microscope MAXYMUS which is located in the UE46-PGM-2 beamline at BESSYII synchrotron (Helmholz-Zentrum Berlin für Materialien und Energie, Germany). The beamline consists of an undulator type insertion device (Apple II) producing X-rays from 130 to 2000 eV[58] which are monochromatized using a plane grating monochromator and focued on a horizontal and vertical exit slit system to provide spatially coherent, monochromatic illumination of the zone plate. The desired diffraction order of the FZP is selected *via* an order selecting aperture (OSA) of the appropriate diameter. A sample is positioned in the focal plane of FZP and is raster scanned with better than 10 nm precision ensured by an interferometer controlled piezoelectric scan stage and a very efficient vibration dampening system. An avalanche photodiode (APD, Hamamatsu, S2382) was utilized as a point detector positioned just behind the sample to record the photon counts at each sample position during raster scan. Prior to imaging experiments, the microscope chamber was flooded with He up to approximately 100 mbar pressure for enhanced heat removal. A Siemens star, (X30-30-1, Xradia, USA) with minimum lines and spaces of 30:30 nm and a certified multilayer made out of alternating GaAs/Al$_{0.7}$Ga$_{0.3}$As layers (Bundesanstalt für Materialforschung und -prüfung, Germany) with a minimum feature size as small as 3.5 nm, were utilized as standard test objects in assessing the resolution performance of the fabricated FZP. The contrast transfer function, CTF, was determined from the integrated intensity value obtained from the marked area in Figure 5a. To achieve this, the image was corrected for its rotation (4°) by using bicubic interpolation. Efficiency measurements were carried out by scanning a 4.4 μm diameter pinhole milled *via* FIB in a ∼6.4 μm gold layer over the FZP and the reference aperture that is positioned 125 μm from the IBL−FZP. To mill this pinhole, a Ga^+ ion beam with 30 kV acceleration voltage, 1 nA current, 50% overlap, and 1.0 μs dwell time was utilized.

Supporting Information Available: Supporting SRIM/TRIM simulation, transmission data, and SEM image. This material is available free of charge *via* the Internet at http://pubs.acs.org.

REFERENCES AND NOTES

1. Kammerer, M.; Weigand, M.; Curcic, M.; Noske, M.; Sproll, M.; Vansteenkiste, A.; Van Waeyenberge, B.; Stoll, H.; Woltersdorf, G.; Back, C. H.; *et al.* Magnetic Vortex Core Reversal by Excitation of Spin Waves. *Nat. Commun.* **2011**, *2*, 279.

2. Van Waeyenberge, B.; Puzic, A.; Stoll, H.; Chou, K. W.; Tyliszczak, T.; Hertel, R.; Fahnle, M.; Bruckl, H.; Rott, K.; Reiss, G.; *et al.* Magnetic Vortex Core Reversal by Excitation with Short Bursts of an Alternating Field. *Nature* **2006**, *444*, 461–464.

3. Vansteenkiste, A.; Chou, K. W.; Weigand, M.; Curcic, M.; Sackmann, V.; Stoll, H.; Tyliszczak, T.; Woltersdorf, G.; Back, C. H.; Schütz, G.; *et al.* X-Ray Imaging of the Dynamic Magnetic Vortex Core Deformation. *Nat. Phys.* **2009**, *5*, 332–334.

4. Mathiesen, R.; Arnberg, L.; Ramsøskar, K.; Weitkamp, T.; Rau, C.; Snigirev, A. Time-Resolved X-Ray Imaging of Aluminum Alloy Solidification Processes. *Metall. Mater. Trans. B* **2002**, *33*, 613–623.

5. Guay, D.; Stewart-Ornstein, J.; Zhang, X.; Hitchcock, A. P. *In Situ* Spatial and Time-Resolved Studies of Electrochemical Reactions by Scanning Transmission X-Ray Microscopy. *Anal. Chem.* **2005**, *77*, 3479–3487.

6. Vila-Comamala, J.; Jefimovs, K.; Raabe, J.; Pilvi, T.; Fink, R. H.; Senoner, M.; Maaßdorf, A.; Ritala, M.; David, C. Advanced Thin Film Technology for Ultrahigh Resolution X-Ray Microscopy. *Ultramicroscopy* **2009**, *109*, 1360–1364.

7. Rehbein, S.; Guttmann, P.; Werner, S.; Schneider, G. Characterization of the Resolving Power and Contrast Transfer Function of a Transmission X-Ray Microscope with Partially Coherent Illumination. *Opt. Express* **2012**, *20*, 5830–5839.

8. Chao, W.; Fischer, P.; Tyliszczak, T.; Rekawa, S.; Anderson, E.; Naulleau, P. Real Space Soft X-Ray Imaging at 10 nm Spatial Resolution. *Opt. Express* **2012**, *20*, 9777–9783.

9. Sakdinawat, A.; Attwood, D. Nanoscale X-Ray Imaging. *Nat. Photonics* **2010**, *4*, 840–848.

10. Kaulich, B.; Thibault, P.; Gianoncelli, A.; Kiskinova, M. Transmission and Emission X-Ray Microscopy: Operation Modes, Contrast Mechanisms and Applications. *J. Phys.: Condens. Matter.* **2011**, *23*, 083002.

11. Thibault, P.; Dierolf, M.; Kewish, C. M.; Menzel, A.; Bunk, O.; Pfeiffer, F. Contrast Mechanisms in Scanning Transmission X-Ray Microscopy. *Phys. Rev. A* **2009**, *80*, 043813.

12. Schütz, G.; Goering, E.; Stoll, H., Synchrotron Radiation Techniques Based on X-Ray Magnetic Circular Dichroism. In *Handbook of Magnetism and Advanced Magnetic Materials*; John Wiley & Sons, Ltd.: New York, 2007.

13. Brizuela, F.; Howlett, I. D.; Carbajo, S.; Peterson, D.; Sakdinawat, A.; Yanwei, L.; Attwood, D. T.; Marconi, M. C.; Rocca, J. J.; Menoni, C. S. Imaging at the Nanoscale with Practical Table-Top EUV Laser-Based Full-Field Microscopes. *IEEE J. Sel. Top. Quantum Electron.* **2012**, *18*, 434–442.

14. Legall, H.; Blobel, G.; Stiel, H.; Sandner, W.; Seim, C.; Takman, P.; Martz, D. H.; Selin, M.; Vogt, U.; Hertz, H. M.; *et al.* Compact X-Ray Microscope for the Water Window Based on a High Brightness Laser Plasma Source. *Opt. Express* **2012**, *20*, 18362–18369.

15. Nagler, B. X-Ray Sources: Tabletop X-Ray Lasers. *Nat. Photon* **2012**, *6*, 719–720.

16. Popmintchev, T.; Chen, M.-C.; Popmintchev, D.; Arpin, P.; Brown, S.; Ališauskas, S.; Andriukaitis, G.; Balčiunas, T.; Mücke, O. D.; Pugzlys, A.; *et al.* Bright Coherent Ultrahigh Harmonics in the keV X-Ray Regime from Mid-Infrared Femtosecond Lasers. *Science* **2012**, *336*, 1287–1291.

17. Chen, M. C.; Arpin, P.; Popmintchev, T.; Gerrity, M.; Zhang, B.; Seaberg, M.; Popmintchev, D.; Murnane, M. M.; Kapteyn, H. C. Bright, Coherent, Ultrafast Soft X-Ray Harmonics Spanning the Water Window from a Tabletop Light Source. *Phys. Rev. Lett.* **2010**, *105*, 173901.

18. Schäfer, D.; Benk, M.; Bergmann, K.; Nisius, T.; Wiesemann, U.; Wilhein, T. Optical Setup for Tabletop Soft X-Ray Microscopy Using Electrical Discharge Sources. *J. Phys.: Conf. Ser.* **2009**, *186*, 012033–012033.

19. Adam, J.-F.; Moy, J.-P.; Susini, J. Table-Top Water Window Transmission X-Ray Microscopy: Review of the Key Issues, and Conceptual Design of an Instrument for Biology. *Rev. Sci. Instrum.* **2005**, *76*, 091301–15.

20. Loosen, P.; Höfer, M.; Esser, D.; Sipma, H.; Kasemann, R. *Proc. Int. Workshop EUV Soft X-Ray Sources 2010* **2010**.

21. Attwood, D. T., *Soft X-Rays and Extreme Ultraviolet Radiation: Principles and Applications*; Cambridge University Press: Cambridge, 2000.

22. Erko, A. I.; Aristov, V. V. e.; Vidal, B., *Diffraction X-Ray Optics*; Institute of Physics Publishing: Philadelphia, 1996.

23. Michette, A. G. *Optical Systems for Soft X Rays*; Plenum Press: New York, 1986.

24. Kirz, J.; Miao, J. David Sayre (1924−2012). *Nature* **2012**, *484*, 38–38.

25. Rehbein, S.; Schneider, G. In *Volume Zone Plate Development at BESSY*; Proc. 8th Int. Conf. X-Ray Microscopy; Institute of Pure and Applied Physics: Tokyo, 2006; pp 103−106.

26. Gorelick, S.; Vila-Comamala, J.; Guzenko, V. A.; Barrett, R.; Salomé, M.; David, C. High-Efficiency Fresnel Zone Plates for Hard X-Rays by 100 keV E-Beam Lithography and Electroplating. *J. Synchrotron Radiat.* **2011**, *18*, 442–446.

27. Vila-Comamala, J.; Pan, Y.; Lombardo, J. J.; Harris, W. M.; Chiu, W. K. S.; David, C.; Wang, Y. Zone-Doubled Fresnel Zone Plates for High-Resolution Hard X-Ray Full-Field Transmission Microscopy. *J. Synchrotron Radiat.* **2012**, *19*, 705–709.

28. Rehbein, S. Nanofabrication of Diffractive Optics for Soft X-Ray and Atom Beam Focusing. *J. Phys. IV* **2003**, *104*, 211–216.

29. Charalambous, P. Developments in the Fabrication of Zone Plates and Other Nanostructures. *AIP Conf. Proc.* **2011**, *1365*, 65–68.

30. Werner, S.; Rehbein, S.; Guttmann, P.; Heim, S.; Schneider, G. Towards High Diffraction Efficiency Zone Plates for X-Ray Microscopy. *Microelectron. Eng.* **2010**, *87*, 1557–1560.

31. Gierak, J. Focused Ion Beam Technology and Ultimate Applications. *Semicond. Sci. Technol.* **2009**, *24*, 043001.

32. Matsui, S.; Kojima, Y.; Ochiai, Y.; Honda, T. High-Resolution Focused Ion Beam Lithography. *J. Vac. Sci. Technol. B.* **1991**, *9*, 2622–2632.

33. Wanzenboeck, H. D.; Waid, S. Focused Ion Beam Lithography. *Recent Advances in Nanofabrication Techniques and Applications, PBC (Ed.), ed. (InTech, 2011)* **2011**.

34. Watt, F.; Bettiol, A.; Van Kan, J.; Teo, E.; Breese, M. Ion Beam Lithography and Nanofabrication: A Review. *Int. J. Nanosci.* **2005**, *4*, 269–286.

35. Cui, Z. *Nanofabrication: Principles, Capabilities and Limits*; Springer: New York, 2008.

36. Baglin, J. E. E. Ion Beam Nanoscale Fabrication and Lithography—a Review. *Appl. Surf. Sci.* **2012**, *258*, 4103–4111.

37. Arshak, K.; Mihov, M.; Arshak, A.; McDonagh, D.; Sutton, D. In *Focused Ion Beam Lithography-Overview and New Approaches*; 24th International Conference on Microelectronics; 16−19 May 2004; IEEE, 2004; vol. 2, pp 459−462.

38. Liddle, J. A.; Gallatin, G. M. Lithography, Metrology and Nanomanufacturing. *Nanoscale* **2011**, *3*, 2679–2688.

39. Nadzeyka, A.; Peto, L.; Bauerdick, S.; Mayer, M.; Keskinbora, K.; Grévent, C.; Weigand, M.; Hirscher, M.; Schütz, G. Ion Beam Lithography for Direct Patterning of High Accuracy Large Area X-Ray Elements in Gold on Membranes. *Microelectron. Eng.* **2012**, *98*, 198–201.

40. Keskinbora, K.; Grévent, C.; Bechtel, M.; Weigand, M.; Goering, E.; Nadzeyka, A.; Peto, L.; Rehbein, S.; Schneider, G.; Follath, R.; *et al.* Ion Beam Lithography for Fresnel Zone Plates in X-Ray Microscopy. *Opt. Express* **2013**, *21*, 11747–11756.

41. Bruchhaus, L.; Bauerdick, S.; Peto, L.; Barth, U.; Rudzinski, A.; Mussmann, J.; Klingfus, J.; Gierak, J.; Hövel, H. High Resolution and High Density Ion Beam Lithography Employing HSQ Resist. *Microelectron. Eng.* **2012**, *97*, 48–50.

42. Tripathi, S. K.; Scanlan, D.; O'Hara, N.; Nadzeyka, A.; Bauerdick, S.; Peto, L.; Cross, G. L. W. Resolution, Masking Capability and Throughput for Direct-Write, Ion Implant Mask Patterning of Diamond Surfaces Using Ion Beam Lithography. *J. Micromech. Microeng.* **2012**, *22*, 055005.

43. Ward, B. W.; Notte, J. A.; Economou, N. P. Helium Ion Microscope: A New Tool for Nanoscale Microscopy and Metrology. *J. Vac. Sci. Technol. B* **2006**, *24*, 2871–2874.

44. Sidorkin, V.; van Veldhoven, E.; van der Drift, E.; Alkemade, P.; Salemink, H.; Maas, D. Sub-10-nm Nanolithography with a Scanning Helium Beam. *J. Vac. Sci. Technol. B* **2009**, *27*, L18–L20.

45. Gierak, J.; Bourhis, E.; Faini, G.; Patriarche, G.; Madouri, A.; Jede, R.; Bruchhaus, L.; Bauerdick, S.; Schiedt, B.; Biance, A. L.; *et al.* Exploration of the Ultimate Patterning Potential Achievable with Focused Ion Beams. *Ultramicroscopy* **2009**, *109*, 457–462.

46. Li, W.-D.; Wu, W.; Williams, R. S. Combined Helium Ion Beam and Nanoimprint Lithography Attains 4 nm Half-Pitch Dense Patterns. *J. Vac. Sci. Technol. B* **2012**, *30*, 06F304–4.

47. Ilinski, P. P.; Lai, B. P.; Bassom, N. J.; Donald, J.; Athas, G. J. In *X-Ray Zone Plate Fabrication Using a Focused Ion Beam*; Proc. SPIE 4145, Advances in X-Ray Optics, January 5, 2001; pp 311−316.

48. Surpi, A.; Valizadeh, S.; Leifer, K.; Lagomarsino, S. Focused Ion Beam Fabrication Procedures of X-Ray Micro Fresnel Zone Plates. *J. Micromech. Microeng.* **2007**, *17*, 617–617.

49. Overbuschmann, J.; Hengster, J.; Irsen, S.; Wilhein, T. Fabrication of Fresnel Zone Plates by Ion-Beam Lithography and Application as Objective Lenses in Extreme Ultraviolet Microscopy at 13 nm Wavelength. *Opt. Lett.* **2012**, *37*, 5100–5102.

50. Lenz, J.; Krupp, N.; Wilhein, T.; Irsen, S. Nanofabrication of Optical Elements for SXR and EUV Applications: Ion Beam Lithography as a New Approach. *AIP Conf. Proc.* **2011**, *1365*, 104–107.

51. Biersack, J.; Ziegler, J. The Stopping and Range of Ions in Solids. In *Ion Implantation Techniques*; Springer: New York, 1982; pp 122−156.

52. Ziegler, J. F.; Ziegler, M. D.; Biersack, J. P. SRIM − the Stopping and Range of Ions in Matter (2010). *Nucl. Instrum. Methods Phys. Res., Sect. B* **2010**, *268*, 1818–1823.

53. Giannuzzi, L. A.; Stevie, F. A., *Introduction to Focused Ion Beams: Instrumentation, Theory, Techniques and Practice*; Springer: New York, 2005.

54. Orloff, J.; Swanson, L.; Utlaut, M. W., *High Resolution Focused Ion Beams: FIB and Its Applications: The Physics of Liquid Metal Ion Sources and Ion Optics and Their Application to Focused Ion Beam Technology*; Springer: New York, 2003.

55. Hopman, W. C. L.; Ay, F.; Hu, W.; Gadgil, V. J.; Kuipers, L.; Pollnau, M.; Ridder, R. M. d. Focused Ion Beam Scan Routine, Dwell Time and Dose Optimizations for Submicrometre Period Planar Photonic Crystal Components and Stamps in Silicon. *Nanotechnology* **2007**, *18*, 195305.

56. Mayer, M.; Grévent, C.; Szeghalmi, A.; Knez, M.; Weigand, M.; Rehbein, S.; Schneider, G.; Baretzky, B.; Schütz, G. Multilayer Fresnel Zone Plate for Soft X-Ray Microscopy Resolves Sub-39 nm Structures. *Ultramicroscopy* **2011**, *111*, 1706–1711.

57. Vladimirsky, Y.; Koops, H. W. P. Moiré Method and Zone Plate Pattern Inaccuracies. *J. Vac. Sci. Technol. B* **1988**, *6*, 2142–2146.

58. Follath, R.; Schmidt, J. S.; Weigand, M.; Fauth, K. The X-Ray Microscopy Beamline UE46-PGM2 at BESSY. *AIP Conf. Proc.* **2010**, *1234*, 323–326.

59. Joy, D. C. Smart − a Program to Measure SEM Resolution and Imaging Performance. *J. Mircrosc.* **2002**, *208*, 24–34.

60. Chen, Y.-T.; Lo, T.-N.; Chu, Y. S.; Yi, J.; Liu, C.-J.; Wang, J.-Y.; Wang, C.-L.; Chiu, C.-W.; Hua, T.-E.; Hwu, Y.; *et al.* Full-Field Hard X-Ray Microscopy Below 30 nm: A Challenging Nanofabrication Achievement. *Nanotechnology* **2008**, *19*, 395302–395302.

61. Michelson, A. A. *Studies in Optics*; Dover Publications, Inc.: New York, 1995.

62. Hecht, E., *Optics*, 4th ed.; Addison Wesley: Reading, MA, 2002.

63. Kirz, J. Phase Zone Plates for X Rays and the Extreme UV. *J. Opt. Soc. Am.* **1974**, *64*, 301–309.

64. Maser, J.; Schmahl, G. Coupled Wave Description of the Diffraction by Zone Plates with High Aspect Ratios. *Opt. Commun.* **1992**, *89*, 355–362.

65. Schneider, G. Zone Plates with High Efficiency in High Orders of Diffraction Described by Dynamical Theory. *Appl. Phys. Lett.* **1997**, *71*, 2242–2244.

66. Schneider, G.; Rehbein, S.; Werner, S. Volume Effects in Zone Plates. In *Modern Developments in X-Ray and Neutron Optics*; Erko, A., Idir, M., Krist, T., Michette, A., Eds.; Springer: Berlin/Heidelberg, 2008; Vol. 137, pp 137−171.

67. Zhang, B.; Seaberg, M. D.; Adams, D. E.; Gardner, D. F.; Murnane, M. M.; Kapteyn, H. C. *Coherent Diffractive Imaging Microscope with a Tabletop High Harmonic EUV Source*; Proc. SPIE 8681, Metrology, Inspection, and Process Control for Microlithography 2013; pp 86810H−86810H-7.

68. Richardson, M. EUV, XUV, and X-Ray Wavelength Sources Created from Laser Plasma Produced from Liquid Metal Solutions, and Nano-Size Particles in Solutions. US20040170252 A1, 2 Sep 2004.

69. Singh, B. *Orion Nanofab: An Overview of Applications*; Carl Zeiss NTS, LLC; New York, 2012.

70. Sai, H.; Tan, K. W.; Hur, K.; Asenath-Smith, E.; Hovden, R.; Jiang, Y.; Riccio, M.; Muller, D. A.; Elser, V.; Estroff, L. A.; *et al.* Hierarchical Porous Polymer Scaffolds from Block Copolymers. *Science* **2013**, *341*, 530–534.

71. Morgan, J.; Notte, J.; Hill, R.; Ward, B. An Introduction to the Helium Ion Microscope. *Microsc. Today* **2006**, *14*, 24–31.

72. Hill, R.; Faridur Rahman, F. H. M. Advances in Helium Ion Microscopy. *Nucl. Instrum. Methods Phys. Res., Sect. A* **2011**, *645*, 96–101.

73. Tennant, D. M. Progress and Issues in E-Beam and Other Top Down Nanolithography. *J. Vac. Sci. Technol. A* **2013**, *31*, 050813–9.

74. Lobo, D. E.; Fu, J.; Gengenbach, T.; Majumder, M. Localized Deoxygenation and Direct Patterning of Graphene Oxide Films by Focused Ion Beams. *Langmuir* **2012**, *28*, 14815–14821.

75. Reyntjens, S.; Puers, R. A Review of Focused Ion Beam Applications in Microsystem Technology. *J. Micromech. Microeng.* **2001**, *11*, 287.

76. Fang, Z.; Lin, C.; Ma, R.; Huang, S.; Zhu, X. Planar Plasmonic Focusing and Optical Transport Using Cds Nanoribbon. *ACS Nano* **2009**, *4*, 75–82.

77. Melli, M.; Polyakov, A.; Gargas, D.; Huynh, C.; Scipioni, L.; Bao, W.; Ogletree, D. F.; Schuck, P. J.; Cabrini, S.; Weber-Bargioni, A. Reaching the Theoretical Resonance Quality Factor Limit in Coaxial Plasmonic Nanoresonators Fabricated by Helium Ion Lithography. *Nano Lett.* **2013**, *13*, 2687–2691.

78. Ögüt, B.; Talebi, N.; Vogelgesang, R.; Sigle, W.; van Aken, P. A. Toroidal Plasmonic Eigenmodes in Oligomer Nanocavities for the Visible. *Nano Lett.* **2012**, *12*, 5239–5244.

79. Schonbrun, E.; Abate, A. R.; Steinvurzel, P. E.; Weitz, D. A.; Crozier, K. B. High-Throughput Fluorescence Detection Using an Integrated Zone-Plate Array. *Lab Chip* **2010**, *10*, 852–856.

80. Schonbrun, E.; Ye, W. N.; Crozier, K. B. Scanning Microscopy Using a Short-Focal-Length Fresnel Zone Plate. *Opt. Lett.* **2009**, *34*, 2228–2230.